

Energy partition of seismic coda waves in layered media: theory and application to Pinyon Flats Observatory

L. Margerin¹, M. Campillo², B.A. Van Tiggelen³, R. Hennino^{*},

¹ *Centre Européen de Recherche et d'Enseignement de Géosciences de l'Environnement, Université Aix Marseille, C.N.R.S.,*

Europôle Méditerranéen de l'Arbois, BP 80, 13545 Aix en Provence, France

² *Laboratoire de Géophysique Interne et Tectonophysique,*

Université Joseph Fourier, C.N.R.S.,

B.P. 53, 38041 Grenoble, France

³ *Laboratoire de Physique et Modélisation de la Matière Condensée,*

Université Joseph Fourier, C.N.R.S.,

Maison des Magistères, 25 avenue des Martyrs,

B.P. 166, 38042 Grenoble, France

SUMMARY

We have studied the partition of shear, compressional and kinetic energies in the coda of ten earthquakes recorded on a dense array, located at Pinyon Flats Observatory (PFO), California. Deformation energies are estimated by measuring finite differences of the wavefield components. We have thoroughly studied the validity and stability of this technique for the PFO data and obtained reliable measurements in the 5-7 Hz frequency band. We observe a clear stabilization of the shear to compressional (W^s/W^p) energy ratio in the coda, with an average value of about 2.8, which

is smaller by a factor 2.5 than the expected ratio at the surface of a homogeneous Poisson half-space. The ratio between the vertical and horizontal kinetic energies (V^2/H^2) can be measured from 5 to 25Hz and shows an abrupt transition from 0.1 in the 5-10Hz band, to about 0.8 in the 15-25Hz band. These measured values are in sharp contrast with the theoretical prediction, around 0.56, for equipartitioned elastic waves in a homogeneous half-space. To explain these observations, we have developed a theory of equipartition in a layered elastic half-space. Using a rigorous spectral decomposition of the elastic wave equation, we define equipartition as a white noise distributed over the complete set of eigenfunctions. This definition is shown to agree with the standard physical concepts in canonical cases. The theory predicts that close to the resonance frequency of a low-velocity layer, the ratio between shear and compressional energies strongly decreases. Using a detailed model of the subsurface at PFO, this counterintuitive result is found to be in good qualitative and quantitative agreement with the observations. Near the resonance frequency of the low-velocity structure, the drop of the energy ratios W^s/W^p and V^2/H^2 is controlled by the change of ellipticity of the Rayleigh wave and the large contribution of the fundamental Love mode. At higher frequencies, the interplay between Rayleigh and Love modes trapped in shallow low-velocity layers is responsible for the abrupt increase of the kinetic energy ratio. Our study demonstrates that the partition of energy in the seismic coda contains information on the local geological structure.

Key words: Coda waves, equipartition, layered media, site effect, eigenfunction expansion

1 INTRODUCTION

Almost forty years ago, Aki (1969) gave the first explanation of the long tail of seismograms. The basic idea is that the diffraction of seismic waves by the heterogeneous crust is at the origin of the late arrivals also known as coda waves. Six years later, Aki & Chouet (1975) proposed the first quantitative explanation for the albedo-exponential decay of the coda with

* formerly at L.G.I.T

time. Two models were proposed: (1) The single scattering approximation in which seismic waves are deflected at a single scattering site during their propagation between source and receiver; (2) The diffusion approximation which basically describes the random walk of the seismic energy in the scattering medium. Although conceptually important, these two models were not sufficiently accurate to model successfully the space time distribution of the energy in the coda. This difficulty was partly overcome when Wu (1985) introduced the acoustic Radiative Transfer Equation (RTE). Mode conversions between P and S waves were later introduced on a phenomenological basis by Zeng (1993) and Sato (1994). The RTE takes into account arbitrary orders of scattering in a rigorous manner, and describes the behavior of intensity in a complex medium beyond the models of single scattering and diffusion. Recently the accuracy of the RTE has been demonstrated by comparisons with full-wave simulations in both acoustic (Wegler et al. 2006) and elastic (Przybilla et al. 2006) media. While the introduction of the RTE in seismology was an important progress, it did not resolve the debate initiated by Aki & Chouet (1975) on the origin of the coda: is it dominated by single or multiple scattering? This question is of both fundamental and practical interest: it is only when the propagation regime is known that it becomes possible to separate scattering from absorption.

In the nineties, the RTE for polarized elastic waves in an inhomogeneous medium has been derived independently by Weaver (1990) and Ryzhik et al. (1996). A particularly interesting outcome of the RTE is the predicted stabilization of the shear (W^s) to compressional (W^p) energy ratio (W^s/W^p) at large lapse time in the coda, independent of the properties of the scatterers. This property is known as equipartition (Weaver 1990; Ryzhik et al. 1996) and was originally proposed by Weaver (1982) to describe diffuse waves, based on statistical physics arguments. Equipartition implies that while the compressional and shear energy decrease exponentially with time, their ratio W^s/W^p tends to a constant. This result was numerically confirmed by Margerin et al. (2000) who found that this behavior can occur after a few scattering events only. A stabilization of the energy ratio W^s/W^p was observed in Mexico by Shapiro et al. (2000) and was found to be in excellent quantitative agreement with an equipartition theory for Rayleigh, Love and body waves by Hennino et al. (2001). The very rapid stabilization of energy ratios observed in Mexico is a clear proof that the propagation of short period elastic waves in tectonically active regions is dominated by multiple scattering.

In this paper, we report the stabilization of the ratio W^s/W^p , and the ratio between vertical and horizontal kinetic energies (V^2/H^2), in the coda of short period seismic waves. The data were collected during a temporary experiment conducted at the Pinyon Flats Observa-

tory (PFO) in California (Fletcher et al. 1990; Vernon et al. 1998), where a small aperture array was installed during six months in 1990. The observed stabilization ratio is around 2.8 which is about 2.5 times smaller than the value expected at the surface of an elastic Poisson half-space (Hennino et al. 2001). To explain this observation we have developed an equipartition theory for elastic waves in a stratified medium. Our approach is based on a spectral decomposition of the elastic operator developed in section 2, which involves generalized eigenfunctions. This technique circumvents the artificial “locked-mode” approximation used by Hennino et al. (2001) and is in much closer agreement with the situation in the Earth. Equipartition can then be defined mathematically as a white noise in the modal space. Using this formal definition, the theoretical results of Weaver (1990) and Hennino et al. (2001) are recovered and generalized to stratified media (section 3). The method avoids mode counting arguments and treats on the same footing surface and body waves. The data analysis and the measurements are presented in section 4. Particular attention has been paid to the stable measurements of partial derivatives of the wavefield. In section 5, we show that equipartition theory in a stratified model of the crust at PFO as proposed by Fletcher et al. (1990) is in good agreement with the observations. In section 6 we conclude and give directions for future research.

2 MATHEMATICAL PRELIMINARIES

In this part we develop formally the spectral decomposition of the elastic wave operator in a stratified half-space. We explain how a complete family of generalized eigenvectors of the elastic wave equation can be constructed, based on scattering theory. The term “generalized” emphasizes the fact that the eigenfunctions are not square integrable, like plane waves. A key result is that any square integrable vector field can be expanded over the set of eigenvectors of the elastic wave equation, which is an important generalization of the Fourier theorem. Detailed calculations and validation of the theory are presented in Margerin (2008).

2.1 General properties of the elastic wave operator

In this part, we summarize results of Dermenjian & Guillot (1985) and Sécher (1998). We consider the following elastic wave equation in \mathbb{R}_-^3 , which denotes the semi-infinite medium $z < 0$. The Lamé parameters λ , μ , and the density ρ are sufficiently well-behaved functions of the position vector \mathbf{x} . For instance, we allow these functions to be discontinuous across smooth boundaries, but we assume that they are bounded away from zero. The elastodynamic

equation reads:

$$\partial_{tt}\mathbf{u}(t) + \mathbf{A}\mathbf{u}(t) = 0, \quad (1)$$

where the operator of elasticity acts on the vector wavefunctions as follows:

$$\mathbf{A}\mathbf{u}_i(\mathbf{x}) = -\frac{1}{\rho(\mathbf{x})}\partial_j(\lambda(\mathbf{x})\partial_k u_k(\mathbf{x})\delta_{ji} + 2\mu(\mathbf{x})\epsilon_{ij}(\mathbf{u})(\mathbf{x})), \quad (2)$$

where ϵ_{ij} is the usual strain tensor:

$$\epsilon_{ij}(\mathbf{u})(\mathbf{x}) = \frac{1}{2}(\partial_i u_j(\mathbf{x}) + \partial_j u_i(\mathbf{x})). \quad (3)$$

According to Dermenjian and Guillot (1988), the operator \mathbf{A} is positive and self-adjoint in the Hilbert space with scalar product:

$$\langle \mathbf{u}, \mathbf{v} \rangle = \int_{\mathbb{R}_-^3} \rho(\mathbf{x}) \mathbf{u}^* \cdot \mathbf{v} d^3x. \quad (4)$$

We will not dwell on the precise definition of the domain of \mathbf{A} . Physically speaking, the choice of the domain ensures that the wavefunctions have finite energy. The spectrum of \mathbf{A} , i.e. the set of generalized eigenvalues of the operator, is the positive real axis and we assume that the Lamé parameters and the density are sufficiently well-behaved so that the spectrum is absolutely continuous (Reed & Simon 1980). In what follows, we briefly explain how to build a complete set of eigenvectors in stratified media using general results from scattering theory in 3-D (Reed & Simon 1979; Ramm 1986). To carry out this task, we first need a basis of eigenvectors for the elastic operator in infinite homogeneous space.

2.2 Eigenvectors of the elastic operator in homogeneous space

In a homogeneous infinite space the elastic operator takes the well-known form:

$$\mathbf{A}_0\mathbf{u} = -\frac{\lambda_0 + 2\mu_0}{\rho_0}\nabla(\nabla \cdot \mathbf{u}) + \frac{\mu_0}{\rho_0}\nabla \times \nabla \times \mathbf{u}. \quad (5)$$

One can verify that plane P waves:

$$\mathbf{e}_{\mathbf{p}}^p(\mathbf{r}) = \frac{\hat{\mathbf{p}}^p}{\rho_0^{1/2}(2\pi)^{3/2}} e^{i\mathbf{p}\cdot\mathbf{r}} \quad (6)$$

are eigenvectors of \mathbf{A}_0 with generalized eigenvalue $p^2\alpha_0^2$, where α_0 denotes the P wavespeed, $\hat{\mathbf{p}}^p$ is a unit vector in the direction of $\mathbf{p} = (p_x, p_y, p_z)$. The term generalized is used to emphasize

the fact that the eigenfunctions are not square integrable. The notational convention used in Equation (6) is as follows: the superscript refers to the wave type and the subscript serves as a label for the eigenfunction. In the case of a continuous spectrum, the label will usually be continuous or sometimes mixed, i.e. discrete+continuous. Similarly, one can introduce two independent S -wave eigenvectors:

$$\mathbf{e}_s^{sh,sv}(\mathbf{r}) = \frac{\hat{\mathbf{p}}^{sh,sv}}{\rho_0^{1/2}(2\pi)^{3/2}} e^{i\mathbf{s}\cdot\mathbf{r}}, \quad (7)$$

where $\hat{\mathbf{p}}^{sh}$ is a unit vector perpendicular to $\hat{\mathbf{s}}$ and the vertical direction $\hat{\mathbf{z}}$, and $\hat{\mathbf{p}}^{sv}$ is a unit vector perpendicular to \mathbf{s} and contained in the (\mathbf{z}, \mathbf{s}) plane. The corresponding eigenvalue is $\beta_0^2 s^2$ where β_0 denotes the shear wave speed. Note that the direction \mathbf{z} is for the moment arbitrary but will be later taken perpendicular to the stratification. The eigenvectors (6)-(7) are orthogonal and have the correct continuum normalisation in the sense of the scalar product (4) defined over \mathbb{R}^3 . Let us verify formally the orthogonality of say \mathbf{e}_s^{sh} and \mathbf{e}_p^p :

$$\begin{aligned} \langle \mathbf{e}_s^{sh} | \mathbf{e}_p^p \rangle &= \int_{\mathbb{R}^3} \rho_0 \frac{\hat{\mathbf{p}}^{sh} \cdot \hat{\mathbf{p}}^p}{\rho_0 (2\pi)^3} e^{i\mathbf{r}\cdot(\mathbf{p}-\mathbf{s})} d^3 r \\ &= \hat{\mathbf{p}}^{sh} \cdot \hat{\mathbf{p}}^p \delta(\mathbf{p} - \mathbf{s}). \end{aligned} \quad (8)$$

The delta function requires that $\mathbf{p} = \mathbf{s}$ in which case the scalar product of the polarization vectors vanishes. Thus the scalar product $\langle \mathbf{e}_s^{sh} | \mathbf{e}_p^p \rangle$ is identically zero. Let us now show formally that our set of eigenvectors is complete, i.e.:

$$\frac{\mathbf{I}\delta(\mathbf{r} - \mathbf{r}')}{\rho_0} = \int_{\mathbb{R}^3} \mathbf{e}_p^p(\mathbf{r}) \mathbf{e}_p^p(\mathbf{r}')^\dagger d^3 p + \int_{\mathbb{R}^3} \mathbf{e}_s^{sh}(\mathbf{r}) \mathbf{e}_s^{sh}(\mathbf{r}')^\dagger d^3 s + \int_{\mathbb{R}^3} \mathbf{e}_{s'}^{sv}(\mathbf{r}) \mathbf{e}_{s'}^{sv}(\mathbf{r}')^\dagger d^3 s', \quad (9)$$

where \mathbf{I} is the identity operator in polarization space: $\mathbf{I}_{ij} = \delta_{ij}$ and the symbol \dagger means hermitian conjugation (conjugate transpose). In equation (9), the normalization prefactor ρ_0^{-1} is a consequence of the definition of the scalar product (4). The sums in the right-hand

side of equation (9) can be written as a single integral:

$$\begin{aligned} \int_{\mathbb{R}^3} \mathbf{e}_{\mathbf{p}}^p(\mathbf{r}) \mathbf{e}_{\mathbf{p}}^p(\mathbf{r}')^\dagger d^3p + \int_{\mathbb{R}^3} \mathbf{e}_{\mathbf{s}}^{sh}(\mathbf{r}) \mathbf{e}_{\mathbf{s}}^{sh}(\mathbf{r}')^\dagger d^3s + \int_{\mathbb{R}^3} \mathbf{e}_{\mathbf{s}'}^{sv}(\mathbf{r}) \mathbf{e}_{\mathbf{s}'}^{sv}(\mathbf{r}')^\dagger d^3s' = \\ \frac{1}{(2\pi)^3 \rho_0} \int_{\mathbb{R}^3} \left(\hat{\mathbf{p}}^p \hat{\mathbf{p}}^{p\dagger} + \hat{\mathbf{p}}^{sh} \hat{\mathbf{p}}^{sh\dagger} + \hat{\mathbf{p}}^{sv} \hat{\mathbf{p}}^{sv\dagger} \right) e^{i\mathbf{p} \cdot (\mathbf{r} - \mathbf{r}')} d^3p = \\ \frac{\mathbf{I}}{2\pi^3 \rho_0} \int_{\mathbb{R}^3} e^{i\mathbf{p} \cdot (\mathbf{r} - \mathbf{r}')} d^3p = \frac{\mathbf{I} \delta(\mathbf{r} - \mathbf{r}')}{\rho_0}, \quad (10) \end{aligned}$$

because the set $(\hat{\mathbf{p}}^p, \hat{\mathbf{p}}^{sh}, \hat{\mathbf{p}}^{sv})$ forms an orthonormal basis in polarization space. We have therefore verified the formal completeness relation.

2.3 Eigenvectors of the elastic wave equation in a stratified half-space

To construct a complete set of eigenvectors in a stratified Earth, we will apply scattering theory. One key idea which can be found e.g. in Reed & Simon (1979) is the following. Let us assume that a complete set of eigenfunctions \mathbf{e}_k^0 of the wave operator \mathbf{A}_0 in a reference medium is known. Now, perturb the reference medium by introducing a localized scattering body to obtain a new operator \mathbf{A} . Then it is possible to show that the eigenvectors \mathbf{e}_k of the perturbed operator are obtained by considering the scattering of \mathbf{e}_k^0 by the heterogeneous body. More precisely, \mathbf{e}_k is the solution of the Lippman-Schwinger equation:

$$\mathbf{e}_k = \mathbf{e}_k^0 + \mathbf{G}^0 \mathbf{A}' \mathbf{e}_k, \quad (11)$$

where \mathbf{G}^0 is the retarded Green function associated with the operator \mathbf{A}_0 . The second term on the right-hand side of equation (11) represents the scattered wave which results from the interaction between an unperturbed incoming wave and the scatterer represented by \mathbf{A}' , a perturbation of \mathbf{A}_0 . The set of eigenvectors constructed in this way is orthogonal and properly normalized (but not necessarily complete). Similar results have been proved for wave scattering by infinite boundaries by Ramm (1986). The construction of a complete basis of eigenvectors for fluids with arbitrary stratification has been conducted by Wilcox (1984). This author demonstrates how the complete set of eigenfunctions can be constructed from the scattering of plane waves incoming from infinity. The method of Wilcox has been used by Dermenjian & Guillot (1985) and Sécher (1998) to construct rigorously a complete basis of eigenfunctions of the elastic operator in a homogeneous half-space with a traction free boundary. Applying the same technique, we can exhibit a complete set of eigenvectors

for a stratified half-space. Complete justification of the formulas below are presented in a separate paper (Margerin 2008). For an alternative approach the reader is referred to Maupin (1996). We assume that as $z \rightarrow -\infty$, the density and Lamé parameters tend to ρ_∞ , λ_∞ and μ_∞ , respectively. The decoupling between SH and (P, SV) motions defines two families of solutions. The case of SH waves is completely similar to the acoustic case described by Wilcox (1984) and will not be discussed. For the $P - SV$ case we take advantage of the translational invariance of the problem and look for solutions of the wave equation which have the following form as $z \rightarrow -\infty$:

$$\psi_{\mathbf{p}}^p(\mathbf{r}) \rightarrow \frac{1}{(2\pi)^{3/2} \rho_\infty^{1/2}} \left(\hat{\mathbf{p}} e^{i\mathbf{p}\cdot\mathbf{r}} + r^{pp} \hat{\mathbf{p}}^r e^{i\mathbf{p}^r\cdot\mathbf{r}} + r^{ps} \hat{\mathbf{p}}^{sv} e^{i\mathbf{s}\cdot\mathbf{r}} \right), \quad (12)$$

where the wavevectors \mathbf{p} , \mathbf{p}^r , and \mathbf{s} have the following properties:

$$\mathbf{p} = (p_x, p_y, p_z), \quad (p_x, p_y) \in \mathbb{R}^2, p_z \in \mathbb{R}^+, \quad (13)$$

$$\mathbf{p}^r = (p_x, p_y, -p_z), \quad (14)$$

$$\mathbf{s} = \left(p_x, p_y, -\sqrt{p_{\parallel}^2 (\alpha_\infty^2/\beta_\infty^2 - 1) + p_z^2 \alpha_\infty^2/\beta_\infty^2} \right), \quad p_{\parallel}^2 = p_x^2 + p_y^2. \quad (15)$$

As before, $\hat{\mathbf{p}}^r$ is a unit vector in the direction of \mathbf{p}^r and $\hat{\mathbf{p}}^{sv}$ is a unit vector orthogonal to \mathbf{s} , contained in the $(\hat{\mathbf{z}}, \mathbf{s})$ plane. The P and S wavespeeds at infinity are denoted by α_∞ and β_∞ , respectively. In equation (12), the dependence of the eigenvector on the wavenumber of the incident wave is emphasized. This equation can be understood as follows: a generalized eigenvector of the operator \mathbf{A} is the sum of an eigenvector of \mathbf{A}_0 , plus the wave back-scattered by the layered structure. The reflection coefficients are determined by the continuity of traction and displacements across interfaces, and by the vanishing of tractions at the free surface. Methods to calculate the reflection matrix R of the layer stack are described in e.g. Kennett (1983) and Aki & Richards (2002). Equation (12) defines eigenvectors of \mathbf{A} with eigenvalue $\omega^2 = \alpha_\infty^2 p^2$. Another family of solution corresponds to incident SV waves from infinity ($z \rightarrow -\infty$):

$$\psi_{\mathbf{s}}^s(\mathbf{r}) \rightarrow \frac{1}{(2\pi)^{3/2} \rho_\infty^{1/2}} \left(\hat{\mathbf{p}}^{sv} e^{i\mathbf{s}\cdot\mathbf{r}} + r^{sp} \hat{\mathbf{p}} e^{i\mathbf{p}\cdot\mathbf{r}} + r^{svsv} \hat{\mathbf{p}}^{svr} e^{i\mathbf{s}^r\cdot\mathbf{r}} \right), \quad (16)$$

where the wavevector \mathbf{p} must be carefully defined, depending on $\mathbf{s} = (s_x, s_y, s_z)$, $s_z > 0$:

$$\mathbf{p} = \begin{cases} \left(s_x, s_y, \sqrt{s_{\parallel}^2 (\beta_\infty^2/\alpha_\infty^2 - 1) + s_z^2 \beta_\infty^2/\alpha_\infty^2} \right) & s_z > s_{\parallel} \sqrt{\frac{\alpha_\infty^2}{\beta_\infty^2} - 1} \\ \left(s_x, s_y, -i\sqrt{s_{\parallel}^2 (1 - \beta_\infty^2/\alpha_\infty^2) - s_z^2 \beta_\infty^2/\alpha_\infty^2} \right) & 0 < s_z < s_{\parallel} \sqrt{\frac{\alpha_\infty^2}{\beta_\infty^2} - 1} \end{cases}, \quad (17)$$

where $s_{\parallel}^2 = s_x^2 + s_y^2$. The eigenvectors (16) have eigenvalues $\omega^2 = \beta_{\infty}^2 s^2$. Note that beyond the critical angle for $SV - P$ mode conversion $-0 < s_z < s_{\parallel} \sqrt{\frac{\alpha_{\infty}^2}{\beta_{\infty}^2} - 1}$, the reflection coefficients as well as the polarization vector $\hat{\mathbf{p}}$ become complex. The reflected P wave is evanescent in the lower half-space, and decays exponentially with depth. The complex polarization vector carries information on the particle motion of P waves in the half-space. Since the vertical component has a $-\pi/2$ phase shift with respect to the horizontal component, the evanescent P wave is in prograde elliptical motion. Equations (12)-(16) define the generalized eigenfunctions that have oscillatory behavior at infinity. However, they do not form a complete set. Similar to bound states that decay rapidly away from a scattering body, the set of eigenvectors must be complemented with surface waves, that have their energy localized near the traction-free surface. In the case of surface waves, the set of eigenvalues is continuous but organized along discrete dispersion branches. The dispersion relation of the surface wave modes can be determined by finding the poles of the reflection coefficients located on the positive real axis. Numerical procedures are described in the books of Kennett (1983) and Aki & Richards (2002). The Rayleigh wave eigenfunctions have the form:

$$\psi_{\mathbf{p}_{\parallel},n}^{Rl}(\mathbf{r}) = \frac{1}{2\pi} \left(\frac{p_x \phi_{(\mathbf{p}_{\parallel},n)}^x(z)}{\sqrt{p_x^2 + p_y^2}}, \frac{p_y \phi_{(\mathbf{p}_{\parallel},n)}^x(z)}{\sqrt{p_x^2 + p_y^2}}, \phi_{(\mathbf{p}_{\parallel},n)}^z(z) \right)^t e^{i(p_x x + p_y y)}, \quad n \in \mathbb{N} \quad (18)$$

where $\phi_{(\mathbf{p}_{\parallel},n)}^x$ and $\phi_{(\mathbf{p}_{\parallel},n)}^z$ denote the horizontal and vertical components of the n^{th} Rayleigh eigenfunction, and obey the following normalization relation:

$$\int_{\mathbb{R}^-} dz \rho(z) \left(\left| \phi_{(\mathbf{p}_{\parallel},n)}^x(z) \right|^2 + \left| \phi_{(\mathbf{p}_{\parallel},n)}^z(z) \right|^2 \right) = 1. \quad (19)$$

These eigenvectors have eigenvalues $\omega_n^2 = c_n(p_{\parallel})^2 p_{\parallel}^2$, where c_n denotes the phase speed of mode n . Note that in equation (18), the surface wave eigenvector is labeled simultaneously with the continuous indices $\mathbf{p}_{\parallel} = (p_x, p_y)$ and the discrete mode branch index n . This means that if we fix the horizontal wavevector \mathbf{p}_{\parallel} and look for solutions of the wave equation that verify simultaneously the traction-free condition and the vanishing of traction and displacements at depth, this can only occur at a discrete set of eigenfrequencies denoted by $\omega_1, \dots, \omega_n, \dots$. Note that in applications, we will work the other way around: the central frequency of the signal is fixed and one looks for poles of the reflection coefficients related to plane waves with apparent velocities smaller than the shear wave velocity in the lower half-space. When a candidate mode has been identified, the Rayleigh quotient is used to calculate its group velocity and as

an accuracy check. In this formulation, it is implicit that the n^{th} mode appears beyond the cut-off frequency ω_n^c .

3 EQUIPARTITION THEORY

3.1 Formal definition of equipartition

Following Shapiro et al. (2000), we introduce the compression and shear deformation energies:

$$W^p = \frac{1}{2} \rho_0 \alpha_0^2 (\nabla \cdot \mathbf{u})^2 \quad (20)$$

$$W^s = \frac{1}{2} \rho_0 \beta_0^2 (\nabla \times \mathbf{u})^2 \quad (21)$$

where α_0 , β_0 and ρ_0 denote the compressional, shear velocity and the density at the receiver, and \mathbf{u} is the displacement vector. Weaver (1982, 1990) and Ryzhik et al. (1996) showed that in a heterogeneous infinite elastic medium, the P to S energy ratio stabilizes at large lapse time:

$$\lim_{t \rightarrow +\infty} \frac{\langle W^s \rangle}{\langle W^p \rangle} = \frac{2\alpha_0^3}{\beta_0^3}, \quad (22)$$

where $\langle \cdot \rangle$ is a statistical averaging over the configuration of scatterers in the medium. This result means that in a heterogeneous medium, multiple scattering creates a partition of compressional and shear energies, which is reached after the waves have encountered a sufficiently large number of scatterers. This is the physical interpretation of the limit $t \rightarrow +\infty$. Remarkably, the equilibration ratio is completely independent of the nature of the scatterer and of the source type.

The result (22) gives no information about the time needed to reach equilibrium. The significance of the limit $t \rightarrow +\infty$ was addressed theoretically by Margerin et al. (2000) and experimentally by Malcolm et al. (2004) and Paul et al. (2005). By solving numerically the elastic radiative transfer equation, Margerin et al. (2000) showed that the asymptotic behavior occurs after a few mean free times only, where the mean free time denotes the average time between two scattering events. These authors also showed that the equilibration time depends on the type of scatterers and the type of source. Therefore, the dynamics of the stabilization process contains information on the medium heterogeneities. It is also important to realize that equilibration is different from equipartition. Equipartition demands that all the modes be represented with equal energies which in turn implies that the flow of energy is isotropic, at least away from medium boundaries (Malcolm et al. 2004). In a recent study, Paul et al. (2005) have shown that equipartition implies equilibration but that the converse statement

is wrong. In particular, Equation (22) applies even when the energy flux distribution is still strongly anisotropic.

It is mathematically convenient to define equipartition as a white noise distributed over all the modes of the system (Weaver 1982; Hennino et al. 2001). In order to illustrate this definition, let us derive the W^s/W^p ratio at equipartition in an infinite homogeneous 3-D medium using the eigenvectors (6)-(7). Completeness implies that the complex vector field \mathbf{u} can be expanded as follows:

$$\mathbf{u}(t, \mathbf{r}) = \int_{\mathbb{R}^3} \mathbf{e}_{\mathbf{p}}^p(\mathbf{r}) e^{-i\omega_{\mathbf{p}}t} d^3p + \int_{\mathbb{R}^3} \left[a_{\mathbf{s}}^{sh} \mathbf{e}_{\mathbf{s}}^{sh}(\mathbf{r}) + a_{\mathbf{s}}^{sv} \mathbf{e}_{\mathbf{s}}^{sv}(\mathbf{r}) \right] e^{-i\omega_{\mathbf{s}}t} d^3s \quad (23)$$

where $\omega_p = \alpha_0 \sqrt{p_x^2 + p_y^2 + p_z^2}$, $\omega_s = \beta_0 \sqrt{s_x^2 + s_y^2 + s_z^2}$. Equation (23) defines the analytic signal associated with the measured displacements. At equipartition, the amplitudes $a_{\mathbf{p}}^p, \dots$ are uncorrelated random variables with zero mean and equal variance. In practice, they are slowly varying functions of time in the frequency band of interest. In order to investigate the energy content at time t in the coda, it is convenient to introduce the Wigner distribution of the wavefield:

$$E_s(t, \tau, \mathbf{r}) = \frac{1}{2} \rho_0 \beta_0^2 \langle \nabla \times \mathbf{u}(t + \tau/2, \mathbf{r}) \cdot \nabla \times \mathbf{u}(t - \tau/2, \mathbf{r})^* \rangle, \quad (24)$$

where $*$ denotes complex conjugation. In equation (24), the brackets denote an ensemble average. Assuming that the coefficients $a_{\mathbf{s}}, a_{\mathbf{p}}$ are governed by a quasi-stationary white-noise process:

$$\langle a_{\mathbf{s}}(t - \tau/2) a_{\mathbf{s}'}^*(t + \tau/2) \rangle = \sigma^2(t) \delta(\mathbf{s} - \mathbf{s}'), \quad (25)$$

one obtains:

$$E_s(t, \tau, \mathbf{r}) = \frac{1}{2} \rho_0 \beta_0^2 \sigma^2(t) \sum_{m=sh,sv} \int_{\mathbb{R}^3} |\nabla \times \mathbf{e}_{\mathbf{s}}^m(\mathbf{r})|^2 e^{-i\omega_{\mathbf{s}}\tau} d^3s. \quad (26)$$

In seismological applications, the function σ models the slow decay of the energy envelope in the coda. The Fourier transform of the Wigner distribution gives the power spectral density at frequency ω_0 :

$$E_s(t, \omega_0, \mathbf{r}) = \frac{1}{2\pi} \int_{-\infty}^{+\infty} E_s(t, \tau, \mathbf{r}) e^{i\omega_0\tau} d\tau \quad (27)$$

$$= \frac{1}{2} \rho_0 \beta_0^2 \sigma^2(t) \sum_{m=sh,sv} \int_{\mathbb{R}^3} |\nabla \times \mathbf{e}_{\mathbf{s}}^m(\mathbf{r})|^2 \delta(\omega_0 - \omega_{\mathbf{s}}) d^3s. \quad (28)$$

The assumption of quasi-stationarity demands that the function σ does not vary significantly during one cycle $2\pi/\omega_0$, where ω_0 is the central frequency of the analyzed signal. Using equation (7), one can show that the squared modulus of the rotational part of the eigenvectors of a homogeneous full-space is independent of position:

$$\left| \nabla \times \mathbf{e}_s^{sh}(\mathbf{r}) \right|^2 = \frac{\omega_0^2}{\rho_0 \beta_0^2 (2\pi)^3}. \quad (29)$$

Introducing spherical polar coordinates to perform the wave number integral in equation (28), one finds the total shear energy spectral density:

$$E_s(t, \omega_0) = \frac{2\sigma^2(t)\omega_0^4}{(2\pi)^2 \beta_0^3}. \quad (30)$$

Using the definition of the compressional energy (20) and following similar lines, one obtains the total compressional energy spectral density:

$$E_p(t, \omega_0) = \frac{\sigma^2(t)\omega_0^4}{(2\pi)^2 \alpha_0^3}, \quad (31)$$

from which the result (22) follows.

3.2 Equipartition in a stratified half-space

In the case of a stratified half-space, calculations have to be performed numerically and in general, the energy ratios depend on depth. Near the boundaries the coupling between P and S waves complicates the physical interpretation of the decomposition of the field energy into shear and compressional components. For instance, Shapiro et al. (2000) have shown that, depending on the incidence angle at the free surface of a homogeneous half-space, a shear wave can generate a large amount of compressional energy and vice-versa. In addition, the sum of compressional and shear energies does not equal the total elastic deformation energy. However, the ratio of shear to compressional energy, as defined above, constitutes a marker of the wave content of the seismic coda. We will also consider the vertical to horizontal kinetic energy ratio. This quantity can be measured without major difficulties on a rather broad frequency range and offers additional information. To illustrate the computational approach, let us for instance consider the contribution of the n^{th} Rayleigh mode to the vertical kinetic energy E_z^{Rl} . Using equation (18) and the property (25), one finds:

$$E_z^{Rl}(t, \omega_0, z) = \frac{\rho(z)\omega_0^2\sigma^2(t)}{8\pi^2} \int_{\mathbb{R}^2} \left| \phi_{(\mathbf{p}_{\parallel}, n)}^z(z) \right|^2 \delta(\omega_0 - \omega_{\mathbf{p}_{\parallel}}) d^2 p_{\parallel}, \quad (32)$$

where $\omega_{\mathbf{p}_{\parallel}} = c_n(\mathbf{p}_{\parallel})p_{\parallel}$, and the vector \mathbf{p}_{\parallel} has components $(p_x, p_y, 0)$. Introducing cylindrical coordinates, the wavenumber integral can be performed to obtain:

$$E_z^{Rl}(t, \omega_0, z) = \frac{\rho(z)\omega_0^3\sigma^2(t)}{c_n u_n 4\pi} \left| \phi_{(p_{\parallel}=\omega_0/c_n, n)}^z(z) \right|^2, \quad (33)$$

where u_n denotes the group velocity of mode n at frequency ω_0 . The transition from equation (32) to (33) uses the following decomposition of the delta function:

$$\delta(\omega_0 - \omega_{\mathbf{p}_{\parallel}}) = \frac{1}{|u_n|} \delta\left(p_{\parallel} - \frac{\omega_0}{c_n}\right). \quad (34)$$

Equation (33) agrees with results of Trégourès & van Tiggelen (2002) who developed a transport theory for elastic waves in a plate. The interpretation of equation (33) is as follows: in the seismic coda, the contribution of the n^{th} Rayleigh mode to the vertical kinetic energy is proportional to the global density of states of the mode and the local value of the wavefunction squared. This product is often referred to as the “local density of states” in the literature (Economou 2005).

It is also instructive to consider the expression of the kinetic energy for the generalized eigenfunctions representing body waves in the lower half-space. For simplicity, we consider the kinetic energy of vertical vibrations E_z^p for the generalized eigenfunctions (12) corresponding to P waves incident from below the sub-surface structure, together with their reflections. To facilitate the comparison with the case of Rayleigh waves, we can rewrite the generalized P wave eigenvector as follows:

$$\psi_{(\mathbf{p}_{\parallel}, p_z)}^p(\mathbf{r}) = \frac{e^{ip_x x + ip_y y}}{2\pi} \phi_{(\mathbf{p}_{\parallel}, p_z)}^p(z), \quad (35)$$

i.e. we split the horizontally and vertically propagating parts. The decomposition (35) highlights the similar roles played by the surface wave mode index n and the vertical wavenumber p_z . Using equations (12) and (25), we obtain the following expression:

$$E_z^p(t, \omega_0, z) = \frac{\rho(z)\omega_0^2\sigma^2(t)}{8\pi^2} \int_0^{+\infty} dp_z \int_{\mathbb{R}^2} \left| \phi_{(\mathbf{p}_{\parallel}, p_z)}^z(z) \right|^2 \delta(\omega_0 - \omega_{(\mathbf{p}_{\parallel}, p_z)}) dp_{\parallel}, \quad (36)$$

where $\omega_{(\mathbf{p}_{\parallel}, p_z)} = \alpha_{\infty} \sqrt{p_x^2 + p_y^2 + p_z^2}$, and $\phi_{(\mathbf{p}_{\parallel}, p_z)}^z$ denotes the vertical component of the generalized P -wave eigenfunction, which depends explicitly on the wavenumbers \mathbf{p}_{\parallel} and p_z . The main difference between equations (36) and (32) is the substitution of the discrete mode branch n with the continuous vertical wavenumber p_z . After introducing cylindrical coordi-

nates, integrating over the vertical wavenumber and the azimuthal angle, one obtains:

$$E_z^P(t, \omega_0, z) = \frac{\rho(z)\omega_0^3\sigma^2(t)}{4\pi\alpha_\infty^2} \int_0^{\omega_0/\alpha_\infty} dp_{\parallel} \frac{p_{\parallel}}{\sqrt{\frac{\omega_0^2}{\alpha_\infty^2} - p_{\parallel}^2}} \left| \phi_{(\mathbf{p}_{\parallel}, p_z)}^z(z) \right|^2 \Big|_{p_z = \sqrt{\frac{\omega_0^2}{\alpha_\infty^2} - p_{\parallel}^2}}, \quad (37)$$

where α_∞ is the P wave speed in the underlying half-space. Upon making the change of variable $p_{\parallel} = \frac{\omega_0}{\alpha_\infty} \sin \theta$, the last equation simplifies to:

$$E_z^P(t, \omega_0, z) = \frac{\rho(z)\omega_0^4\sigma^2(t)}{4\pi\alpha_\infty^3} \int_0^{\pi/2} d\theta \sin \theta \left| \phi_{(\mathbf{p}_{\parallel}, p_z)}^z(z) \right|^2 \Big|_{\left(p_{\parallel} = \frac{\omega_0}{\alpha_\infty} \sin \theta, p_z = \frac{\omega_0}{\alpha_\infty} \cos \theta\right)}. \quad (38)$$

Evaluated at $z = 0$ in the case of a homogeneous half-space, equation (38) reduces to similar expressions obtained by Weaver (1985), based on physical reasoning. Note that away from the free surface, the eigenmodes of the system do not reduce to pure P or S waves but consist of a superposition of incident and reflected body waves. The result (38) can be interpreted as follows: the contribution of generalized P eigenfunctions to the kinetic energy of vertical vibrations is proportional to the density of states of P waves in the lower half-space and to the squared P -wavefunction, averaged over all possible directions of P -waves incident from below the structure. Note that the last integral (38) also depends on depth and, in general, presents complicated oscillations. This is illustrated in Figure 1 where kinetic and deformation energy ratios are plotted as a function of depth in a homogeneous 3-D Poisson half-space. The largest fluctuations of the deformation and kinetic energy ratios occur in the vicinity of the free surface and are mostly caused by the depth dependence of the Rayleigh wave eigenfunction. When averaged over one shear wavelength λ_s at a depth greater than $3\lambda_s$, the energy ratios reduce to the expected values for a homogeneous infinite medium. Our calculations are in perfect agreement with previous work by Hennino et al. (2001); Trégourès & van Tiggelen (2002), based on a locked-mode method. The present approach is generally valid for an arbitrarily stratified half-space. Experimentally, the V^2/H^2 kinetic energy ratio is fairly easy to measure over a broad frequency range but can be strongly affected by the local topography. The ratio of deformation energies W^s/W^p is more difficult to evaluate but is independent of the choice of local coordinate system. It is therefore expected to be less sensitive to geometrical effects. In the next section, we discuss the measurement of the deformation energy ratio on a dense array.

4 STABILIZATION OF DEFORMATION ENERGY RATIOS IN THE SEISMIC CODA

4.1 Data set and pre-processing

The data we use were collected by a temporary array that was deployed at the Pinyon Flats Observatory (PFO) in 1990. This array operated as part of the Incorporated Research Institutions for Seismology (IRIS), and was located in Southern California between the San Jacinto and the San Andreas fault, as shown on the location maps in Figure 2

The array was composed of 58 sensors arranged in a six-sensor by six-sensor grid with 200m long arms. The sensors were 2Hz L22-D geophones with an acquisition sampling frequency of 250Hz. They were triggered by two borehole sensors located at 275m and 150m depth, respectively. A total of 300 events was recorded, among which 140 were located with good accuracy. In our study, we have used 10 events whose source parameters are described in Table 1. These earthquakes have epicentral distances smaller than 50km and magnitudes higher than 2. We chose these events because they exhibit a pronounced coda with a high signal to noise ratio. We took care of filtering out the frequency components above 40Hz because the signal exhibits significant instrumental noise around 60Hz. Because the estimate of the divergence and curl of the wavefield requires the application of the traction-free boundary condition (Shapiro et al. 2000), we must first define geometrically the free surface. For this purpose we chose the plane which best approximates the location of stations in a least-squares sense. The data were rotated in a new reference system whose vertical axis is directed perpendicular to the optimal plane. The signal components were detrended and normalized to equal root mean square amplitude at each station i :

$$\forall i \in \{1, \dots, n\}, \quad \begin{cases} \int u_z(\mathbf{r}_i, t)^2 dt = \bar{u}_z^2 \\ \int u_{ew}(\mathbf{r}_i, t)^2 dt = \bar{u}_{ew}^2 \\ \int u_{ns}(\mathbf{r}_i, t)^2 dt = \bar{u}_{ns}^2 \end{cases}, \quad (39)$$

where the bar denotes the root mean square. This normalisation procedure corrects for possible instrumental response differences and yields more reliable estimates for the field derivative.

4.2 Method of estimation for P and S energies

To estimate the deformation energies W^p and W^s , the displacement gradients $\partial_i u_j$ of the wavefield need to be measured. We will first examine the problem of estimating the horizontal

derivatives. These will be subsequently used to obtain the vertical derivatives. Using three or four stations as shown in Figure 3, the derivative of the wavefield in two linearly independent horizontal directions can be estimated, which suffices to recover the horizontal components of the gradient vector by application of the Taylor expansion formula:

$$u(\mathbf{r}_2) \approx u(\mathbf{r}_1) + (\mathbf{r}_2 - \mathbf{r}_1) \cdot \nabla u + O(|\mathbf{r}_2 - \mathbf{r}_1|^2). \quad (40)$$

In practice, the estimate of the spatial derivative requires a great coherence of the displacements at two near-by stations. Applying a finite difference approximation to equation (40), one finds

$$\frac{\partial u_i}{\partial x_j} \approx \frac{u_i(\mathbf{r}_1 + d\mathbf{j}) - u_i(\mathbf{r}_1)}{d}, \quad (41)$$

where d is the inter-station distance. $u_i(\mathbf{r}_1 + d\mathbf{j})$ and $u_i(\mathbf{r}_1)$ correspond to the measured displacements at positions $\mathbf{r}_2 = \mathbf{r}_1 + d\mathbf{j}$ and \mathbf{r}_1 , respectively. The approximation (41) will be correct provided $d/\lambda \ll 1$ and its application to the data set will be critically examined. Following Shapiro et al. (2000), we use the free surface boundary condition to express the derivative in the z direction in terms of horizontal derivatives:

$$\begin{cases} \partial_z u_x = -\partial_x u_z \\ \partial_z u_y = -\partial_y u_z \\ \partial_z u_z = -(1 - 2\beta^2/\alpha^2)(\partial_x u_x + \partial_y u_y) \end{cases}.$$

It follows that the divergence and curl of the wavefield can be expressed in terms of derivatives along horizontal coordinates exclusively

$$\nabla \cdot \mathbf{u} = 2\frac{\beta^2}{\alpha^2}(\partial_x u_x + \partial_y u_y), \quad (42)$$

$$\nabla \times \mathbf{u} = (2\partial_y u_z, -2\partial_x u_z, \partial_x u_y - \partial_y u_x). \quad (43)$$

We now study the validity of our estimates of spatial derivatives in the data. Practically, we approximate $\partial_x u_x$ with the finite-difference formula (41). The estimate is based on the assumption that the two signals are very similar, i.e., the change of waveform between two stations is infinitesimal. Using the converse assumption we propose a method to determine the limit of validity of the finite difference approximation. When two signals are poorly correlated the following result applies: $\langle u_i(1)u_i(2) \rangle \ll \bar{u}_i^2$. Therefore we can obtain the following estimate

of the derivative for incoherent signals

$$\begin{aligned} \sqrt{\frac{\langle (u_i(2) - u_i(1))^2 \rangle}{d^2}} &= \frac{\sqrt{\langle u_i^2(2) \rangle + \langle u_i^2(1) \rangle - 2\langle u_i(1)u_i(2) \rangle}}{d} \\ &\approx \frac{\sqrt{2} \bar{u}_i}{d} \end{aligned} \quad (44)$$

Therefore we expect to find a $1/d$ behavior when the signals at 2 stations are poorly correlated, i.e. sufficiently far apart. Figure 4 shows the finite difference $\frac{u_i(\mathbf{r}_1+d\mathbf{j})-u_i(\mathbf{r}_1)}{d}$ as a function of inter-station distance d . In the 5 – 7Hz frequency band, and for distances shorter than 50m, the evaluation is unstable because the time shifts between the two waveforms becomes nearly equal to the sampling period. For distances greater than 150m, we roughly find the predicted $1/d$ behavior (see equation (44)). For inter-station distances ranging from 50m to 150m, the finite difference curve shows a plateau, indicating that the measurement is stable and reliable. In order to avoid possible biasing by extreme values that sometimes appear, we define the experimental derivative as the median of all available finite difference values.

4.3 Stabilization of shear to compressional energy ratios

Compressional (W^p) and shear (W^s) energies have been measured for each event and for different frequency bands. Figure 5 shows a typical example of the band-pass filtered signal between 5 and 7 Hz, the decay of energies with time, and the dynamics of the ratio between shear and compressional energies. For this event a stabilization of the energy ratio is clearly visible in the coda. While the total energy itself decreases by two orders of magnitude, the ratio shows remarkably weak fluctuations. In addition, we infer that the stabilization occurs very rapidly, only a few cycles after the arrival of the direct S wave. When the compressional energy W^p reaches the background noise level, the energy ratio again fluctuates randomly and stabilization disappears. This observation indicates that the wave contents of noise and coda are rather different. In a sense, the coda is easier to interpret because it is likely to contain an equipartition mixture of all the modes of the system. Because fluctuations are weak, we define the stabilization ratio as the average of W^s/W^p over a time window starting one second after the direct S arrival and ending when W^p is of the order of the noise level. The equilibration has been observed for the ten earthquakes provided that frequencies lower than 3 Hz and greater than 9 Hz have been removed. The low frequency coda is difficult to measure because of the poor sensitivity of the sensors. At too high frequencies the diffuse field is not sufficiently coherent to obtain reliable estimates of the derivatives. The results are shown in Figure 6, where we illustrate the fact that the equipartition ratio is independent

of the source parameters. This favors an interpretation of the observed stabilization as a consequence of multiple scattering. However, the equilibration ratio equals 2.8 ± 0.4 , which is much lower than the ratio 7.2 predicted at the surface of a homogeneous Poisson half-space (Figure 1). A likely explanation is the non-uniformity of velocities in the upper crust. The seismic properties under the PFO array have been studied by Fletcher et al. (1990) and Vernon et al. (1998). These authors have shown that the first 50 to 70 meters at Pinyon Flats are composed of weathered granite with low seismic velocities. At greater depth, intact granite with high wavespeeds is found. Therefore, we speculate that the anomalously low energy ratio at PFO is caused by the presence of low-velocity layers. We further explore this hypothesis by applying equipartition theory in stratified media.

5 MODELING ENERGY RATIOS IN THE CODA

The structure under the PFO array was explored by Fletcher et al. (1990) and Vernon et al. (1998). We first study a simplified model of the velocity and density profiles, composed of a thin layer (65 m thickness) with relatively low velocities (2.77 km/s for P -wave and 1.6 km/s for S -wave) overlying a half-space with typical crustal velocities (5.2 km/s for P -wave and 3 km/s for S -wave). The elastic medium is poissonian everywhere and the density is uniform. The properties of the different seismic models studied in this paper are summarized in Table 2. In Figure 7, the frequency dependent theoretical ratio between shear (W^s) and compressional (W^p) energies at equipartition is represented. At low frequency, the waves are insensitive to the thin low-velocity layer and the 7.2 ratio of a homogeneous Poisson half-space is recovered. At low frequency, the fundamental Love wave can be completely neglected, and the largest contribution to the S and P deformation energies is made first by the Rayleigh waves, and second by the generalized eigenfunctions representing body waves in the lower half-space. At very high frequency the W^s/W^p ratio again converges to the half-space value. This is not so surprising, since we may expect the diffuse wavefield to be rather insensitive to the deep velocity contrast. The pronounced drop of the energy ratio to values smaller than 4 around the fundamental resonance frequency of the layer is largely due to the change of the Rayleigh wave ellipticity and the increasing importance of the fundamental Love mode near the resonance frequency of the layer. At high frequencies, the generalized eigenfunctions corresponding to body waves in the underlying half-space play little role in the equipartition ratio. The high-frequency oscillations are mostly due to the interplay between Rayleigh and Love waves.

Because the deformation energies are accessible in a narrow frequency band only, we have

also evaluated the ratio of vertical (V^2) to horizontal (H^2) kinetic energies in the 5-25 Hz band. The measurement of this ratio is straightforward and offers additional information on the local structure. The experimental results are plotted in Figure 8 and show a clear frequency dependence. The ratio decreases from 0.5 at frequencies around 4 Hz to about 0.1-0.2 in the 6-12Hz frequency band, then rapidly increases to 0.8, and oscillates around this value in the 15-25Hz frequency band. While a simplified 1-layer model (model 1 in Table 2) gives a clear qualitative explanation of the observations at PFO, it is not quantitatively satisfactory. By a process of trial and error and using a-priori information provided by previous studies, we tried to find 2-layer models that better match the observation. The velocity and density profile of a typical 2-layer model is given in Table 2. The velocities in the bedrock and in the deepest part of the weathered zone are identical to those given by Fletcher et al. (1990). According to these authors the near-surface seismic properties are more variable and less well constrained. Therefore we explored various thicknesses and velocities for the top layer. Regarding the density, little information could be found in the literature. We adopted a typical value of 2.7 for the intact bedrock and allowed the density to decrease to 2.2 in the weathered, less consolidated layers. Observed and theoretical energy ratios for a 2-layer model that fits reasonably well the W^s/W^p and V^2/H^2 ratios up to 15 Hz are shown in Figure 8. In the simple 2-layer model, the small V^2/H^2 ratio at low frequency is due simultaneously to the nearly horizontal polarization of the fundamental mode Rayleigh wave and the increasing role played by the fundamental Love wave. For a thorough study of the frequency-dependent ellipticity of the Rayleigh wave in layered structures, the reader is referred to Malischewsky & Scherbaum (2004). In model 2 (see Table 2), at frequencies higher than 5 Hz, the surface waves trapped in the low-velocity layers largely dominate over body waves coming from below the structure. The sharp increase of the V^2/H^2 ratio at high-frequencies is again explained by an interplay between Love and Rayleigh waves. Around 15 Hz, the fundamental mode Rayleigh wave becomes strongly vertically polarized and the weight of Love waves in the equipartition ratio suddenly drops. The two effects combined explain the peak value observed in the data. Calculations based on Rayleigh waves only, predict fluctuations of the V^2/H^2 ratio much bigger than observed. This demonstrates that the contribution of Love waves is of fundamental importance. At frequencies higher than 15Hz, the measured kinetic energy ratio oscillates and departs significantly from the model calculations. This may indicate a departure from the simple layered structure.

By exploring a large number of models, we found that the position of the steep rise from the low to high frequency behavior is extremely sensitive to the the thickness and velocity

of the upper layer. This is illustrated in Figure 9 where the frequency dependent vertical to horizontal kinetic ratio has been measured at one station located at the end of one of the two orthogonal arms (see Figure 2). Figure 9 also shows the calculations of the frequency dependent ratio between the vertical and horizontal kinetic energies for model 3, Table 2. This model is completely similar to model 2, except in the first 15 meters where the velocities are slightly different from those proposed by Fletcher et al. (1990). This model fits reasonably well the observations over the whole frequency band. The comparison of Figures 8 and 9 demonstrates that the frequency dependence of the ratio between vertical and horizontal kinetic energies measured in the coda contains information on the local velocity structure. In the case of PFO, our study supports the idea that the velocity profile presents simultaneously velocity gradients at depth and thin very low-velocity layers at the surface.

6 CONCLUSION AND OUTLOOK

We have observed the stabilization of ratios of deformation and kinetic energies in the coda of small earthquakes, at PFO. The stabilization phenomenon is interpreted as a sign of multiple scattering of waves in the crust at high frequencies. The ratio between the shear and compressional energies can be accurately estimated in the 5-7 Hz frequency band and was observed to be much lower than the one found in Mexico by Shapiro et al. (2000). To understand this observation, we have developed a theory of equipartition in arbitrary layered elastic media based on the spectral decomposition of the elastodynamic operator. We have shown that the decrease of the S to P deformation energy ratio may be explained by the low-velocity subsurface layers. Like in Mexico (Shapiro et al. 2000; Hennino et al. 2001), the stabilization of various energy ratios occurs shortly after the S wave arrival. Such a rapid stabilization has also been found in numerical simulations (Margerin et al. 2000), typically after a moderate number (3-4) of scattering events. This suggests that the mean free time -the typical time between two scattering events- is very small, of the order of a few seconds only, and supports the idea of a highly heterogeneous crust in California. Our results on the frequency dependence of the ratio of vertical to horizontal kinetic energies sound reminiscent of the so-called Nakamura's technique which relies on the frequency dependence of the H/V spectral ratio of ambient noise vibrations (see Bard 1998, for a review). This technique usually makes use of the low-frequency H/V peak to retrieve the resonance frequency of sedimentary deposits. The physical bases and limitations of the H/V method are still actively debated. Bonnefoy-Claudet et al. (2006) present a detailed study of a simple 1-layer configuration which illustrates the complex interpretation of H/V measurements depending on the spatial distribution of the noise

sources. Because coda waves are composed of an equipartitioned mixture of all modes, they are in a sense easier to model than noise signals. We have shown that it is possible to model reasonably well the frequency dependent ratio of vertical to horizontal kinetic energies in the coda at PFO. In addition to a low-frequency global resonance of the 1-D structure, we find that some information on the uppermost layers can also be obtained. Another interesting aspect of the coda is the possibility to check the wave content of the signal through the measurements of several energy ratios that can be compared to theoretical predictions. Further investigations of site effect assessments with coda waves are required before reaching more definitive conclusions.

REFERENCES

- Aki, K., 1969. Analysis of the Seismic Coda of Local Earthquakes as Scattered Waves, *J. Geophys. Res.*, **74**, 6215–6231.
- Aki, K. & Chouet, B., 1975. Origin of coda waves: Source, attenuation, and scattering effects, *J. Geophys. Res.*, **80**, 3322–3342.
- Aki, K. & Richards, P. G., 2002. *Quantitative seismology, theory and methods*, University Science Books.
- Bard, P.-Y., 1998. Microtremor measurement: a tool for site effect estimation?, in *The Effects of Surface Geology on Seismic Motion*, pp. 1251–1279, Balkema, Rotterdam.
- Bonnefoy-Claudet, S., Cornou, C., Bard, P. Y., Cotton, F., Moczo, P., Kristek, J., & Fäh, D., 2006. H/V ratio: a tool for site effects evaluation. results from 1-d noise simulations, *Geophys. J. Int.*, **167**, 827–837.
- Dermenjian, Y. & Guillot, J.-C., 1985. Les ondes élastiques dans un demi-espace isotrope. Développement en fonctions propres généralisées. Principe d’absorption limite., *C. R. Acad. Sci. Paris. Ser. I. Math.*, **301**, 617–619.
- Economou, E. N., 2005. *Green’s functions in quantum physics*, Springer-Verlag.
- Fletcher, J. B., Fumal, T., Liu, H., & Porcella, R., 1990. Near-surface velocities and attenuation at two bore-holes near Anza, *Bull. Seism. Soc. Am.*, **80**, 807–831.
- Hennino, R., Trégourès, N., Shapiro, N. M., Margerin, L., Campillo, M., van Tiggelen, B. A., & Weaver, R. L., 2001. Observation of Equipartition of Seismic Waves, *Phys. Rev. Lett.*, **86**, 3447–3450.
- Kennett, B. L. N., 1983. *Seismic wave propagation in stratified media*, Cambridge University Press.
- Malcolm, A. E., Scales, J. A., & van Tiggelen, B. A., 2004. Extracting the Green function from diffuse, equipartitioned waves, *Phys. Rev. E*, **70**, 015601.
- Malischewsky, P. G. & Scherbaum, F., 2004. Loves formula and H/V-ratio (ellipticity) of Rayleigh waves, *Wave Motion*, **40**, 57–67.
- Margerin, L., 2008. Normal modes of layered elastic media and application to diffuse fields, <http://fr.arXiv.org/abs/0803.0204v1>, last accessed on March 3, 2008.
- Margerin, L., Campillo, M., & Van Tiggelen, B., 2000. Monte Carlo simulation of multiple scattering of elastic waves, *J. Geophys. Res.*, **105**, 7873–7892.
- Maupin, V., 1996. The radiation modes of a vertically varying half-space - a new representation of the complete Green’s function in terms of modes, *Geophys. J. Int.*, **126**, 762–780.
- Paul, A., Campillo, M., Margerin, L., Larose, E., & Derode, A., 2005. Empirical synthesis of time-asymmetrical Green functions from the correlation of coda waves, *J. Geophys. Res.*, **110**(B9), B08302.
- Przybilla, J., Korn, M., & Wegler, U., 2006. Radiative transfer of elastic waves versus finite difference simulations in two-dimensional random media, *J. Geophys. Res.*, **111**, B04305.

- Ramm, A. G., 1986. *Scattering by obstacles*, D. Reidel Publishing Company.
- Reed, M. & Simon, B., 1979. *Scattering theory*, vol. 3 of **Methods of Mathematical Physics**, Academic Press, New York.
- Reed, M. & Simon, B., 1980. *Functional analysis*, vol. 1 of **Methods of Mathematical Physics**, Academic Press, New York.
- Ryzhik, L. V., Papanicolaou, G. C., & Keller, J. B., 1996. Transport Equations for Elastic and Other Waves in Random Media, *Wave Motion*, **24**, 327–370.
- Sato, H., 1994. Multiple Isotropic Scattering Model Including P-S Conversions For the Seismogram Envelope Formation, *Geophys. J. Int.*, **117**, 487–494.
- Sécher, P., 1998. Étude spectrale du système différentiel 2×2 associé à un problème d'élasticité linéaire, *Annales de la faculté des sciences de Toulouse*, **7**, 699–726.
- Shapiro, N. M., Campillo, M., Margerin, L., Singh, S. K., Kostoglodov, V., & Pacheco, J., 2000. The energy partitioning and the diffusive character of the seismic coda, *Bull. Seism. Soc. Am.*, **90**, 655–665.
- Trégourès, N. P. & van Tiggelen, B. A., 2002. Quasi-two-dimensional transfer of elastic waves, *Phys. Rev. E*, **66**(3), 036601.
- Vernon, F. L., Pavlis, G. L., Owens, T. J., Macnamara, D. E., & Anderson, P. N., 1998. Near-surface scattering effects observed with a high-frequency phased array at Pinyon Flats, California, *Bull. Seism. Soc. Am.*, **88**, 1548–1560.
- Weaver, R. L., 1982. On diffuse waves in solid media, *J. Acoust. Soc. Am.*, **71**, 1608–1609.
- Weaver, R. L., 1985. Diffuse elastic waves at a free surface, *J. Acoust. Soc. Am.*, **78**, 131–136.
- Weaver, R. L., 1990. Diffusivity of ultrasound in polycrystals, *J. Mech. Phys. Solids*, **38**, 55–86.
- Wegler, U., Korn, M., & Przybilla, J., 2006. Modeling Full Seismogram Envelopes Using Radiative Transfer Theory with Born Scattering Coefficients, *Pure and Applied Geophysics*, **163**, 503–531.
- Wilcox, C., 1984. *Sound propagation in stratified fluids*, vol. 50 of **Applied Mathematical Sciences**, Springer-Verlag, Berlin and New York.
- Wu, R. L., 1985. Multiple scattering and energy transfer of seismic waves - separation of scattering effect from intrinsic attenuation - I. Theoretical modeling, *Geophys. J. R. Astron. Soc.*, **82**, 57–80.
- Zeng, Y., 1993. Theory of scattered P- and S-wave energy in a random isotropic scattering medium, *Bull. Seism. Soc. Am.*, **83**, 1264–1276.

Origin time	Latitude	Longitude	Magnitude	Depth	Source-array distance(km)
117.12.52.42.392	34.0487	-116.3908	2.3	-2.2	48.89
118.08.32.38.165	33.8647	-116.1659	2.4	5.1	39.04
122.11.35.03.691	33.4927	-116.4624	2.1	7.0	13.20
125.08.10.15.667	33.5074	-116.4672	2.0	8.3	11.64
127.12.40.57.581	33.8693	-116.1555	2.0	3.7	40.08
130.07.23.35.987	33.6496	-116.7291	2.1	15.7	25.46
130.14.25.10.270	33.1944	-116.3622	2.8	14.5	47.13
132.23.54.49.190	33.9839	-116.3103	2.5	4.8	43.50
134.05.05.27.123	33.5384	-116.6073	2.6	11.8	16.01
136.01.14.21.003	33.4376	-116.4491	2.4	11.1	19.30

Table 1. Location and magnitude of the 10 events used in this study.

Model 1	Model 2	Model 3
		$h_1 = 4\text{m}$
		$\alpha_1 = 300\text{m/s}$
		$\beta_1 = 150\text{m/s}$
		$\rho_1 = 2200\text{kg/m}^3$
	$h_1 = 11\text{ m}$	
	$\alpha_1 = 720\text{m/s}$	
	$\beta_1 = 400\text{m/s}$	$h_2 = 11\text{m}$
$h_1 = 65\text{m}$	$\rho_1 = 2200\text{kg/m}^3$	$\alpha_2 = 900\text{m/s}$
$\alpha_1 = 2770\text{m/s}$		$\beta_2 = 500\text{m/s}$
$\beta_1 = 1600\text{m/s}$		$\rho_2 = 2200\text{kg/m}^3$
$\rho_1 = 2700\text{kg/m}^3$	$h_2 = 41\text{ m}$	
	$\alpha_2 = 3100\text{m/s}$	
	$\beta_2 = 1600\text{m/s}$	$h_3 = 50\text{m}$
	$\rho_2 = 2500\text{kg/m}^3$	$\alpha_3 = 3100\text{m/s}$
		$\beta_3 = 1600\text{ m/s}$
		$\rho_3 = 2700\text{kg/m}^3$
$\alpha_\infty = 5200\text{m/s}$	$\alpha_\infty = 5400\text{m/s}$	$\alpha_\infty = 5400\text{m/s}$
$\beta_\infty = 3000\text{m/s}$	$\beta_\infty = 3000\text{m/s}$	$\beta_\infty = 3000\text{m/s}$
$\rho_\infty = 2700\text{ kg/m}^3$	$\rho_\infty = 2700\text{kg/m}^3$	$\rho_\infty = 2700\text{kg/m}^3$

Table 2. Seismological models of the sub-surface at Pinyon Flats Observatory used in this study. The different depths and velocities are inspired by the results of Fletcher et al. (1990).

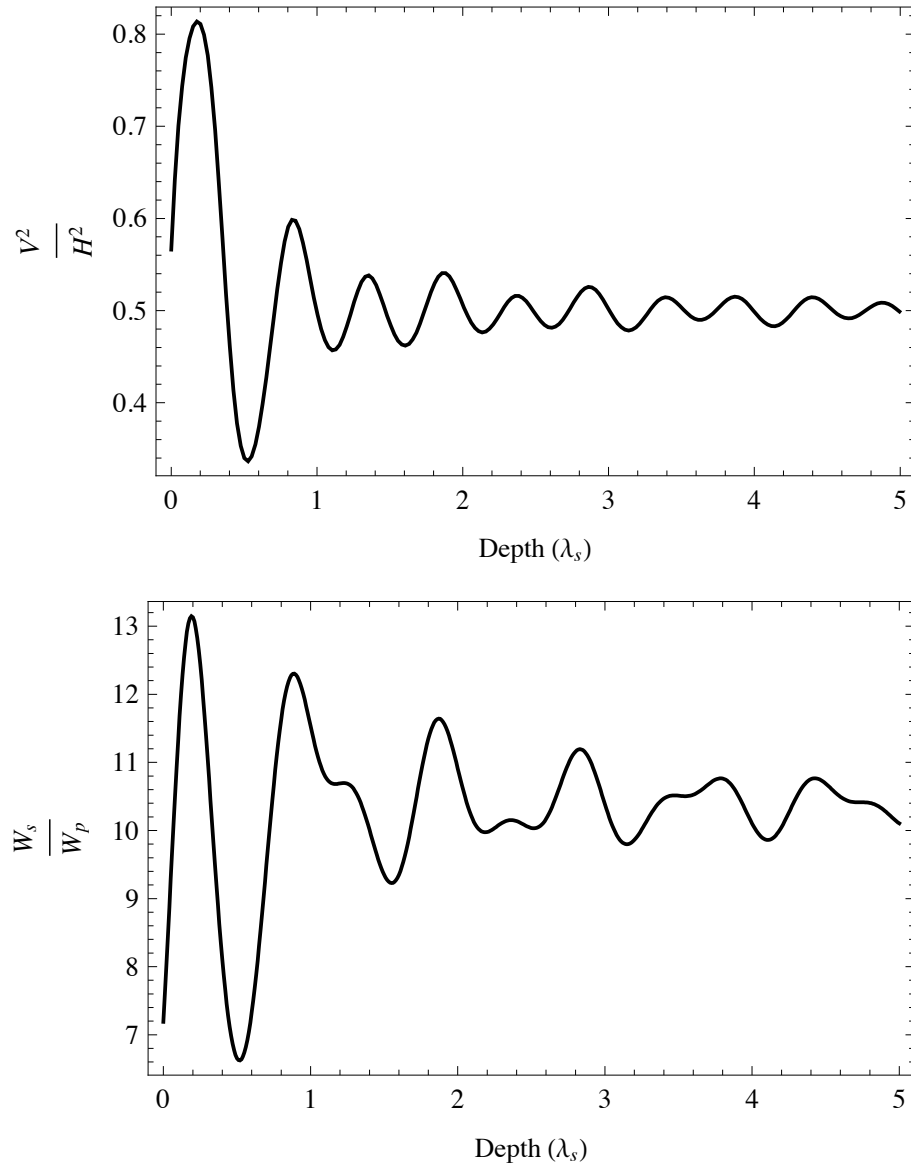


Figure 1. Depth dependence of energy ratios at equipartition in a homogeneous elastic half-space (Poisson solid). The depth unit is the shear wavelength λ_s . Top: vertical to horizontal kinetic energy ratio. Bottom: shear to compressional deformation energy ratio. Note the persistent oscillations at depth, which originate from the interference between incident and reflected waves at the free surface.

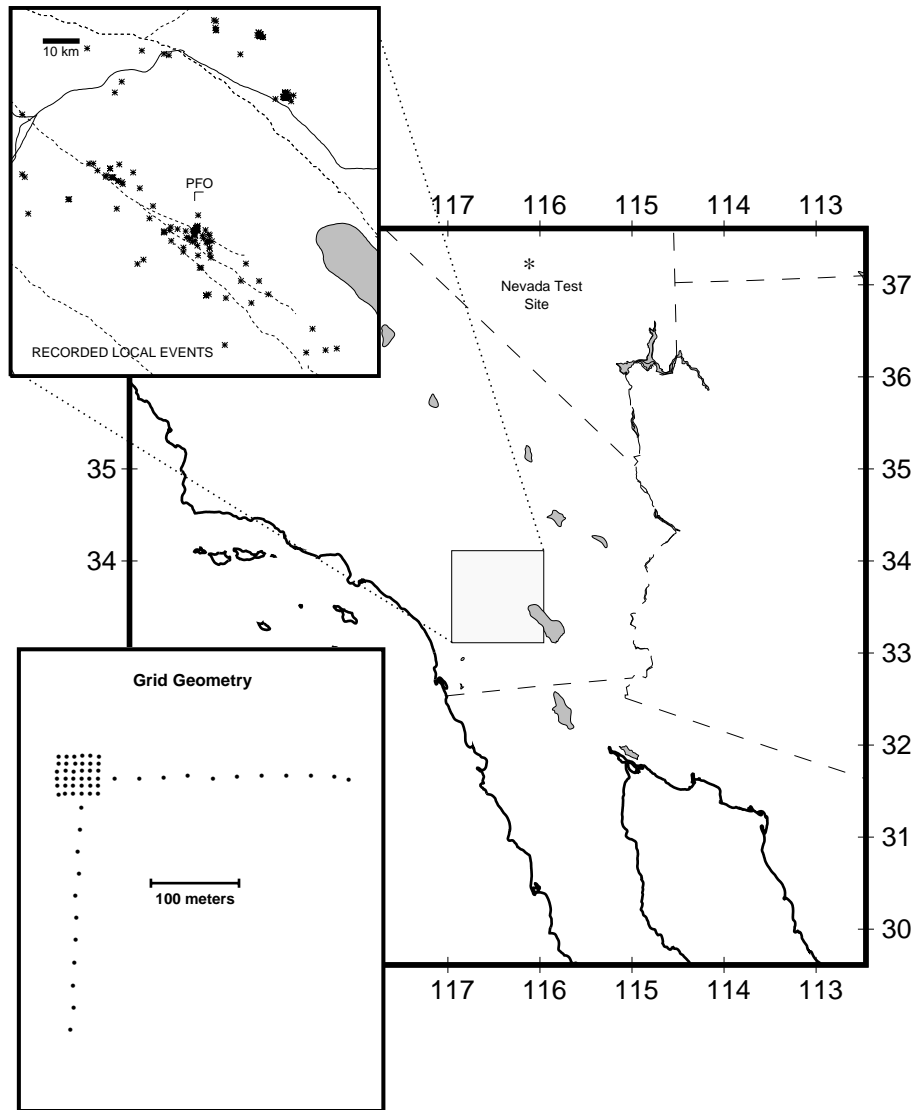


Figure 2. Location map of the 1990 Pinyon Flats High Frequency Array Experiment. 58 3-components sensors were deployed during 3 months. The upper-left inset shows the location of the largest magnitude local events recorded by the array. The lower-left inset shows the acquisition geometry: a dense square of 6×6 seismometers separated by 7 meters, and two perpendicular long arms composed of 11 seismometers separated by 21 meters. Reproduced from Vernon et al. (1998)

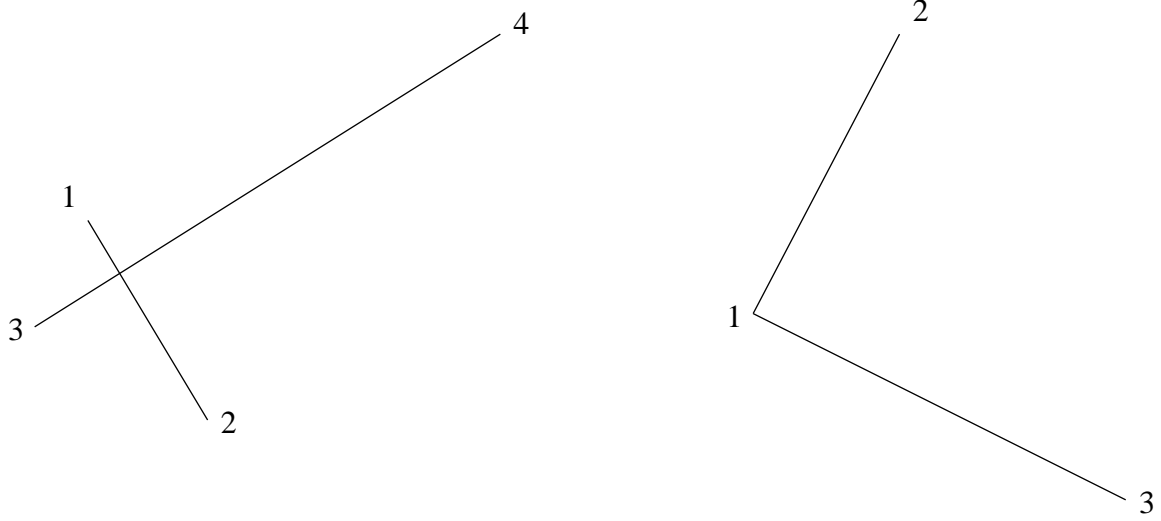


Figure 3. Estimation of the divergence and curl of the wavefield requires the measurement of the derivative along two linearly independent directions. This figure presents two valid configurations with 3 or 4 stations

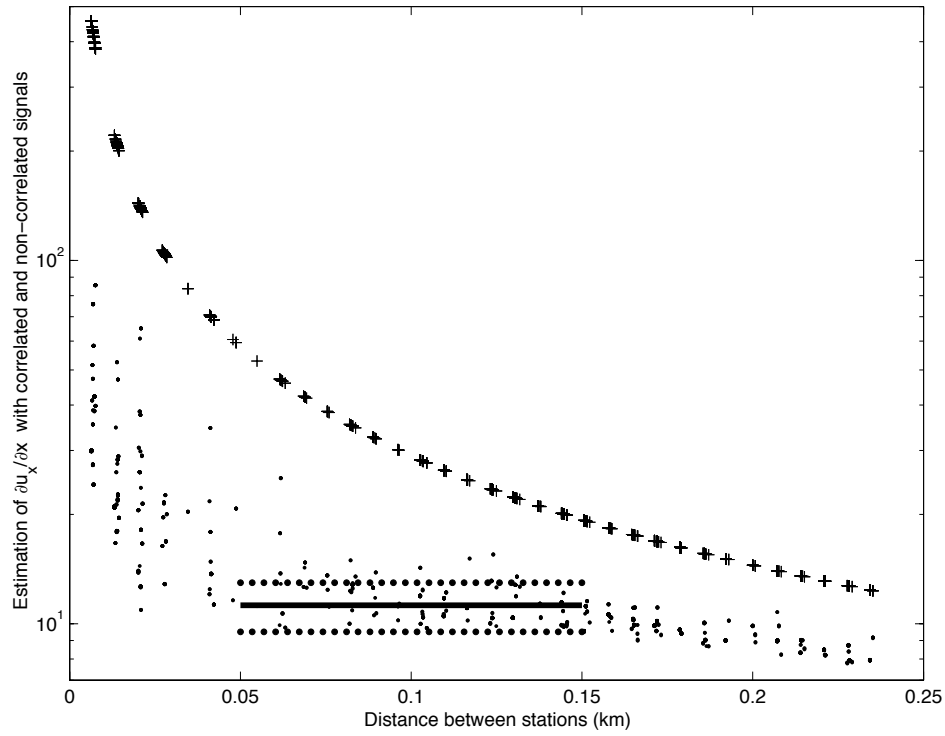


Figure 4. Measurement of the spatial derivative of the wavefield on a dense array of seismometers. Dots: estimates of the derivative $\partial u_z / \partial x$ for one event at lapse time $t = 32.4$ s. The mean value of the field derivative is indicated by a solid line. The horizontal dotted lines indicate the plus or minus one standard deviation range. The + symbols show the estimate of the derivative for incoherent fields. The plot illustrates the stability of the estimate of the derivative for stations located at least 50m and at most 150m apart. Beyond this distance the field at the two stations become uncorrelated as shown by the coincidence between the incoherent and coherent estimates of the wavefield derivative.

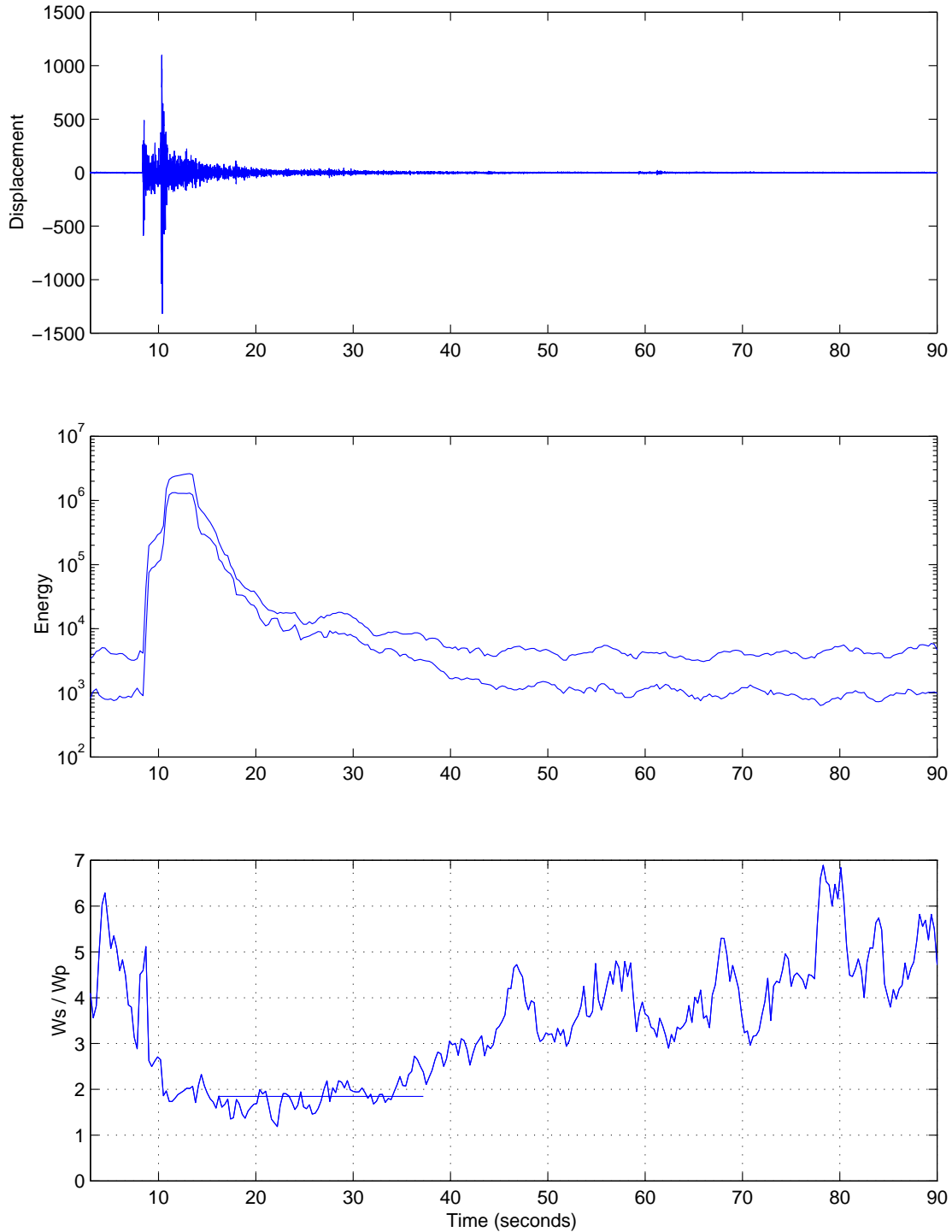


Figure 5. Observation of the stabilization of deformation energies in the seismic coda. Top : example of vertical displacement for a shallow magnitude 2.0 local event. Middle : compressional and shear deformation energies as a function of time. Note the logarithmic scale on the vertical axis. Bottom : time dependence of the shear to compressional energy ratio. The ratio shows small random fluctuations while the total energy decays by two orders of magnitude. Note the large fluctuations of energy ratios in the noise following the coda. The horizontal line indicates the time window used to estimate the stabilization value.

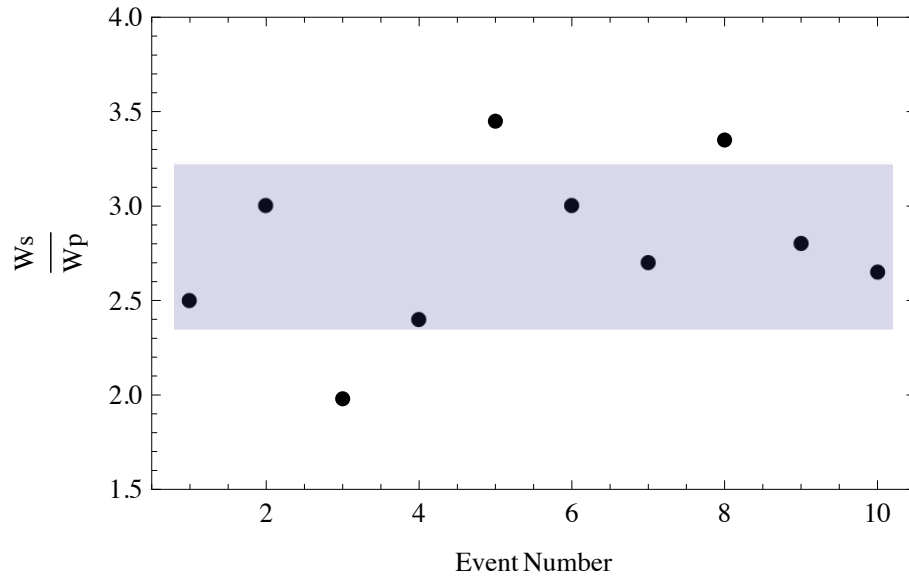


Figure 6. Estimate of shear to compressional energy ratios for 10 local events in the 5–7Hz frequency band. The stabilization ratio varies little from one event to the other. The shaded region indicates plus or minus one standard deviation around the mean value. This feature agrees with the theoretical prediction that the energy ratio in the coda is independent from the source parameters.

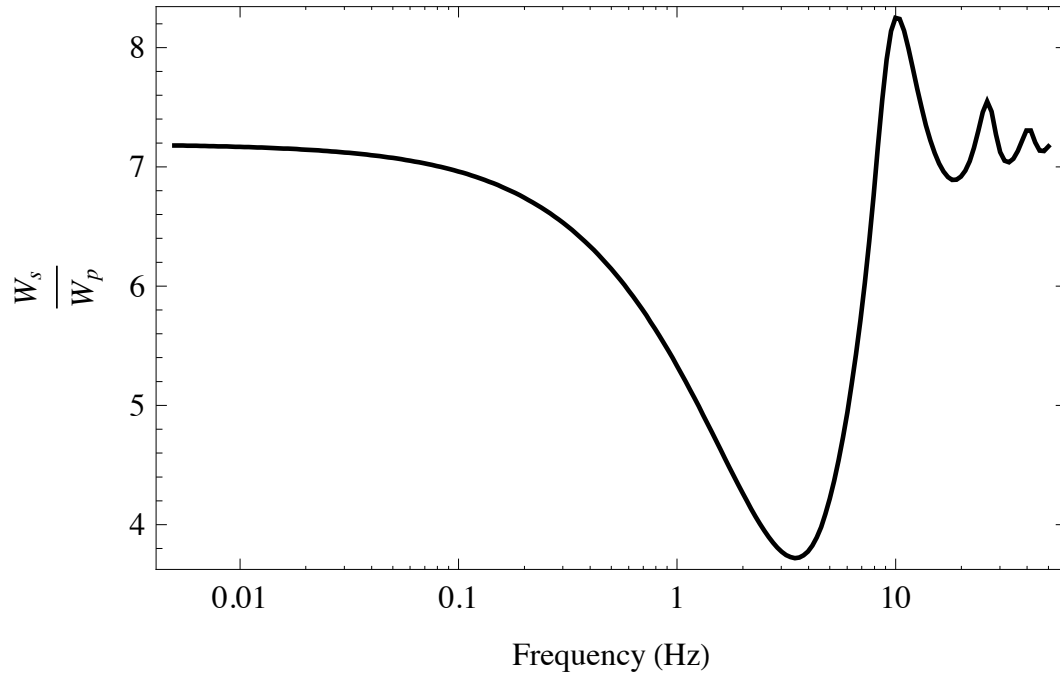


Figure 7. Frequency dependence of the equipartition ratio between shear (W_s) and compressional (W_p) energies in a one-layer model of Pinyon Flats Observatory. At a depth of 65m, the shear velocity increases by a factor almost 2 (model 1 in Table 2). At low and high-frequencies, the equipartition ratio of a Poisson half-space is recovered. Close to the resonance frequency of the low-velocity layer, a significant drop of the ratio W_s/W_p is observed.

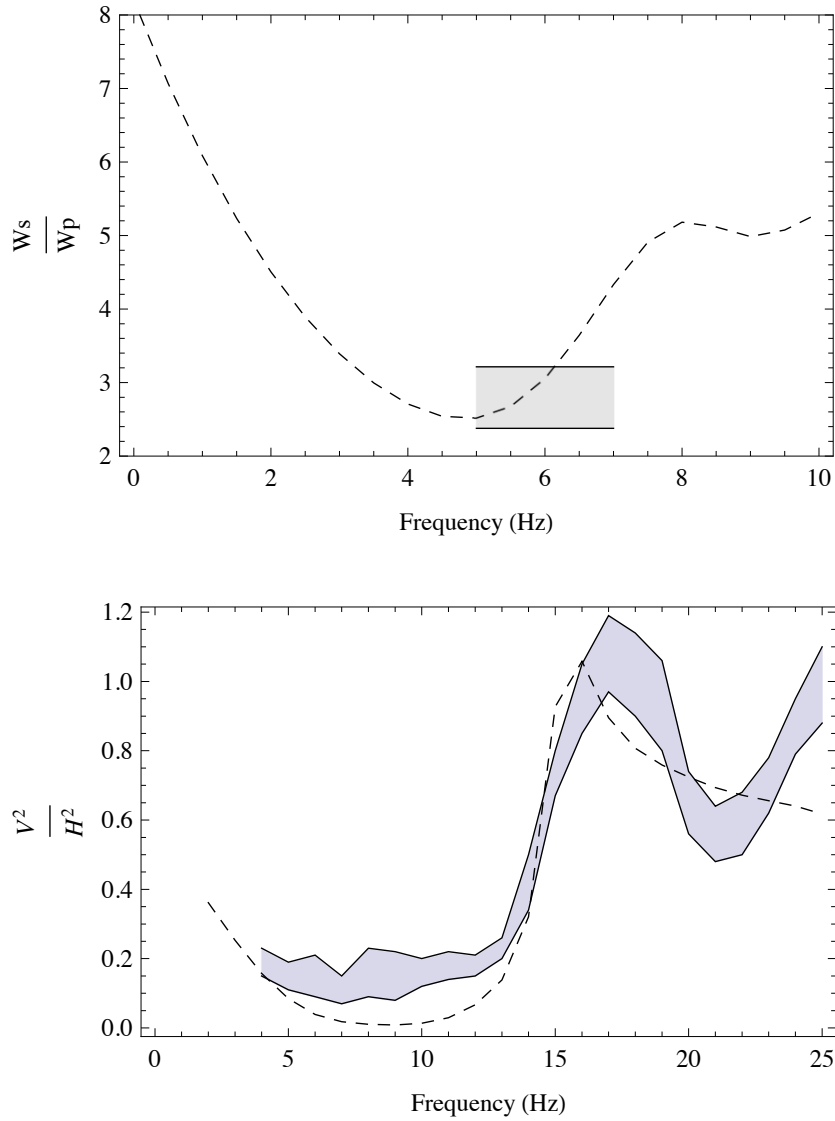


Figure 8. Modeling of the measured stabilization ratios with a simple 2-layer model of PFO as described in Table 2 (model 2). Top: Observed (shaded region) and modeled (dashed line) shear to compressional energy ratio. Bottom: Observed (shaded region) and modeled (dashed line) vertical to horizontal kinetic energy ratio. The black solid lines delimit the ± 1 standard deviation region around the mean value. Agreement is reasonable up to 15 Hz.

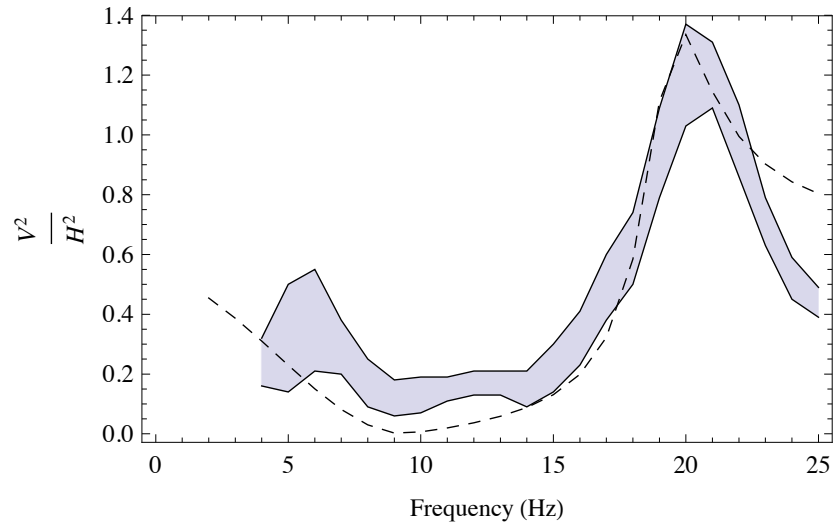


Figure 9. Modeling of the measured stabilization ratio between vertical and horizontal kinetic energies with a 3-layer model of PFO as described in Table 2 (model 3). The shaded area delimits the ± 1 standard deviation region for the data. The dashed line shows the model calculations.